INTERNATIONAL JOURNAL FOR NUMERICAL METHODS IN FLUIDS, VOL. 5, 463–481 (1985)

A THREE-LEVEL GENERALIZED-CO-ORDINATE GROUP FINITE-ELEMENT METHOD FOR COMPRESSIBLE VISCOUS FLOW

K. SRINIVAS AND C. A. J. FLETCHER

Department of Mechanical Engineering, University of Sydney, NSW 2006, Australia

SUMMARY

A consistent three-level time-split group finite-element method, suitable for the computation of viscous compressible flows in irregular geometric domains, is described. Exploitation of the group[12] formulation permits an accurate and economical algorithm to be developed in a generalized-co-ordinate (ξ, η) space. A variable sweep cycle is used to accelerate convergence to the steady state. The method is demonstrated by computing laminar and turbulent flow past a trailing edge. The method uses an algebraic eddy viscosity model to represent turbulence and produces results in close agreement with the experiments and computations of Viswanath *et al.*[8]

KEY WORDS Trailing-edge Flow Laminar Flow Turbulent Flow Generalized Co-ordinates Group Finite-element Method

1. INTRODUCTION

Transonic flow about the trailing edge of an aerofoil offers considerable challenge to the computational fluid dynamicist. The flow is complicated because of the dominance of the viscous–inviscid interaction, large adverse streamwise pressure gradients together with large pressure gradients normal to the aerofoil surface. Further, one has the interaction of different shear layers in the near wake. These effects influence, significantly, the design of an aerofoil and assume particular importance in the case of supercritical aerofoils.

Any attempt to compute such a flow is made more complicated by the geometry of the trailing edge. One would like to have a rectangular and uniform mesh in the computational domain. Though certain geometries, such as that of a flat plate or a backward-facing step, allow the prescription of a rectangular mesh there are many other geometries, such as a complete aerofoil or even just the trailing edge of an aerofoil, which do not allow the prescription of a rectangular mesh. Further, in many of the computations of physical interest there are regions with sharp gradients of the flow variables, for example the near-wake, where one has to prescribe a fine mesh to achieve a good spatial resolution. In such a case it may be prohibitively expensive to use a fine mesh throughout the computational domain. The mesh should be fine in regions where sharp gradients exist and coarse elsewhere.

Despite these complexities, there have been some attempts to compute trailing-edge flows. Recently, Horstman[1,2] has computed the turbulent flow about an asymmetric trailing-edge and has provided a detailed comparison of the computed results with those of experiments. He has solved the unsteady, Reynolds-averaged Navier–Stokes equations and has used various models of turbulence. The k–ε and k–ω^2 models have been shown to provide results in good agreement with experiments. The recent MacCormack scheme[3] has been used to solve the equations.

0271–2091/85/050463–19$01.90

Received 4 May 1984
Revised 6 November 1984

Diewert[4] has obtained the flow around a complete aerofoil using MacCormack's explicit-implicit-characteristics method[5] and different models of turbulence. Baker *et al.*[6] have considered the complete aerofoil geometry to compute incompressible flow past the trailing edge. They employ the steady-state equations and the k–ε model of turbulence. The equations have been solved by using a finite-element formulation. Rhie and Chow[7] employ a finite-volume method with the k–ε turbulence model and find that the accuracy of the results is highly dependent on the degree of resolution of the strong trailing-edge gradients.

There have also been a few experimental studies of the flow over the trailing edge of an aerofoil, notably those of Viswanath *et al.*[8], Cleary *et al.*[9] and Viswanath and Brown.[10]

In this paper we present a *time-split group* finite-element method in generalized co-ordinates to compute flows where the physical domain would require a distorted mesh, e.g. a trailing-edge flow. For the application of the conventional finite-element method on a distorted mesh, it has been usual to employ an isoparametric formulation. Using this formulation, the distorted mesh in the physical domain is mapped into a uniform mesh in the transform plane, *after* discretization.

But it is well known that the isoparametric formulation, though conceptually convenient, can lead to inaccuracies if the elements are too distorted.[11] Here we follow an alternative path by expressing the equations in generalized co-ordinates (ξ, η), *prior* to discretization. The Galerkin *group* finite-element method[12] with linear Lagrange elements is then applied in the (ξ, η) plane. The set of resulting ordinary differential equations is converted into an efficient computational algorithm by the application of a *consistent* time-split formulation[13] in the (ξ, η) plane. The nodal transformation parameters, i.e. the Jacobians, carry all the information about the physical domain. The resulting formulation is both more accurate and more economical than the isoparametric formulation.

The deliberate use of the *group* finite-element formulation[12] is another feature of the present work. Such a formulation avoids the computationally inefficient treatment of the convective terms by the conventional finite-element method. An operation count estimate[12] shows that in the present case, which features cubic non-linearities, the group formulation is approximately seventeen times more economical than the conventional finite-element method. This large gain in economy is expected to be accompanied by a small gain in accuracy, based on numerical experiments with the two-dimensional Burgers' equation.[14]

The use of the group formulation with Lagrange elements permits *directional mass and difference operators* to be isolated[15] and, in turn, facilitates the construction of the consistent time-split formulation. Although in the present investigation a pseudo-transient technique is used to obtain the steady-state solution, the consistent time-split formulation is also suitable for problems where the transient solution is of direct interest.

The directional mass operators are smoothing operators and are the source of the increased accuracy associated with the finite-element method. The present finite-element formulation applied to the Euler equations produces a fourth-order scheme on a uniform mesh; whereas the equivalent finite-difference scheme, i.e. with lumped mass operators[13] would be only second-order accurate. The present formulation permits the mass operators to be included with a relatively small operational overhead.

Further, we replace the two-level (in time) time-split scheme[16] by a three-level scheme which is more robust and which converges to the steady state more quickly.[13] The resulting time-split finite-element method will compute efficiently laminar or turbulent flow in an irregular domain due to three specific features:

(i) the group finite-element formulation[12]
(ii) consistent three-level time-split algorithm[13]
(iii) the implementation of the Galerkin finite element method in the transform (ξ, η) plane.

The scheme to be presented is a development of the ADI finite-element method[16,17] which was used, together with an eddy viscosity model for turbulence, to compute flows past a flat plate and a backward-facing step. Results in good agreement with other computational and experimental results were obtained.

Here, we apply the generalized-co-ordinate time-split finite-element scheme to compute laminar and turbulent flows past a trailing edge. Trailing-edge flow is a member of a class of problems which requires a considerable number of iterations, and hence substantial execution time, to converge. In this paper, we describe a 'variable sweep cycle' which gives a considerable reduction in execution time.

The rest of this paper is as follows. Section 2 introduces the governing equations and the eddy viscosity turbulence model to be employed. The three-level time-split algorithm is developed in Section 3. The application of the method to the trailing-edge flows is discussed in Section 4. We study in particular velocity profiles, displacement thickness and surface pressure distributions. Section 4 also includes a discussion of the 'variable sweep cycle' and results obtained with its application.

2. GOVERNING EQUATIONS

The flow is governed by the two-dimensional, compressible, Navier–Stokes equations. In the Cartesian co-ordinates these are

$$\frac{\partial \mathbf{q}}{\partial t}+\frac{\partial \mathbf{F}}{\partial x}+\frac{\partial \mathbf{G}}{\partial y}=\frac{\partial^2 \mathbf{R}}{\partial x^2}+\frac{\partial^2 \mathbf{S}}{\partial x \partial y}+\frac{\partial^2 \mathbf{T}}{\partial y^2}, \tag{1}$$

where

$$\begin{aligned}
\mathbf{q} &= \{\rho, \rho u, \rho v\},\\
\mathbf{F} &= \{\rho u, p+\rho u^2-\sigma_x, \rho u v-\tau_{xy}\},\\
\mathbf{G} &= \{\rho v, \rho u v-\tau_{xy}, p+\rho v^2-\sigma_y\},\\
\mathbf{R} &= \{\theta^{\mathrm{d}}_{\rho}\rho, \tfrac{4}{3}\mu u, \mu v\},\\
\mathbf{S} &= \left\{0, \frac{\mu}{3}v, \frac{\mu}{3}v\right\},\\
\mathbf{T} &= \{\theta^{\mathrm{d}}_{\rho}\rho, \mu u, \tfrac{4}{3}\mu v\},\\
\sigma_x &= \tfrac{4}{3}\varepsilon u_x-\tfrac{2}{3}\varepsilon v_y,\\
\sigma_y &= \tfrac{4}{3}\varepsilon v_y-\tfrac{2}{3}\varepsilon u_x,\\
\tau_{xy} &= \varepsilon(u_y+v_x),
\end{aligned} \tag{2}$$

ρ = density, u, v = velocity components in x and y directions, p = pressure, $\sigma_x, \sigma_y, \tau_{xy}$ = Reynolds stresses, μ = molecular viscosity, ε = eddy viscosity (see Section 2.2 for details), $\theta^{\mathrm{d}}_{\rho}\rho$ (non-dimensional $\theta = 10/Re$) are the dissipative terms included in the continuity equation to stabilize the numerical procedure.

It is assumed that the temperature changes in the solution domain are small. Such an assumption is justified for the flows of interest, which are transonic. As a consequence, the molecular viscosity, μ, is assumed to be constant everywhere. Further, the following relationship between pressure and velocity is assumed:[16]

$$p=\rho\left\{RT_0-\frac{\gamma-1}{2\gamma}(u^2+v^2)\right\}. \tag{3}$$

Because of equation (3) the energy equation (not shown above) need not be solved.

The equations are non-dimensionalized with respect to a characteristic length L, free stream velocity u_∞ and free stream density ρ_∞. Then μ is replaced in equation (2) by $1/Re$ where Re is the Reynolds number $\left(\frac{\rho_\infty u_\infty L}{\mu}\right)$. The non-dimensional form of the pressure equation (i.e. equation (3)) is

$$1+\gamma M_\infty^2 p=\rho\left\{1+\frac{\gamma-1}{2}M_\infty^2(1-u^2-v^2)\right\}, \tag{4}$$

where M_∞ is the free-stream Mach number.

2.1. *Transformation of the governing equations*

In the present study a distorted mesh is required adjacent to the trailing edge. In a finite-element framework it is usual to use an isoparametric formulation[18] to map the distorted mesh in the physical plane into a uniform mesh in the transform plane. However this transformation takes place after the spatial discretization (by applying the finite element method) in the physical plane. The result is a computationally expensive evaluation of integral expressions for the algebraic coefficients. This integration is usually carried out numerically using Gauss quadrature in the transform plane. Although this is more economical than carrying out the integration in the physical plane it is still an expensive process unless only first derivatives appear and linearly. In this case, the Jacobian associated with the first derivative cancels with the Jacobian associated with the integration and the numerical integration can be carried out once and for all.[15]

For the conventional finite-element treatment of the convective terms the Gauss quadrature must be repeated at each iteration or at each time step unless the algebraic coefficients are evaluated once and for all and stored. In addition it is known[11] that if the mesh in the physical plane is very distorted the solution accuracy deteriorates.

In the present study the distorted mesh in the physical plane is transformed into a rectangular mesh in the transform plane *before* the group finite-element formulation is introduced. The governing equations include transformation parameters but can be written in a form that is not significantly more complicated (see equation (7)) than the form of the equations in the physical plane. By applying the group finite-element formulation[12] in the transform (ξ,η) plane the resulting algorithm is both more accurate and more economical than applying the conventional finite-element method with an isoparametric mapping.

The general transformation is introduced via

$$\xi=\xi(x,y),\quad \eta=\eta(x,y). \tag{5}$$

Under this transformation,

$$u_x=\xi_x u_\xi+\eta_x u_\eta,\quad u_y=\xi_y u_\xi+\eta_y u_\eta,\text{etc.} \tag{6}$$

Upon transforming equation (1) to the (ξ,η) plane, using equation (5) one gets

$$\mathbf{q}_t^*+\mathbf{F}_\xi^*+\mathbf{G}_\eta^*-\mathbf{R}_{\xi\xi}^*-S_{\xi\eta}^*-\mathbf{T}_{\eta\eta}^*=0, \tag{7}$$

where

$$\mathbf{q}^{*t}=\left\{\frac{\rho}{J},\frac{\rho u}{J},\frac{\rho v}{J}\right\}, \tag{8}$$

$$\mathbf{F}^* = \frac{1}{J}\begin{bmatrix} \rho U_c \\ \xi_x p + \rho u U_c + \left(\frac{4\mu}{3}\xi_{xx} + \mu\xi_{yy}\right)u + \left(\frac{\mu}{3}\xi_{xy}\right)v - \xi_x\sigma_x - \xi_y\tau_{xy} \\ \xi_y p + \rho v U_c + \left(\mu\xi_{xx} + \frac{4\mu}{3}\xi_{yy}\right)v + \left(\frac{\mu}{3}\xi_{xy}\right)u - \xi_x\tau_{xy} - \xi_y\sigma_y \end{bmatrix}, \tag{9}$$

$$\mathbf{G}^* = \frac{1}{J}\begin{bmatrix} \rho V_c \\ \xi_x p + \rho u V_c + \left(\frac{4\mu}{3}\eta_{xx} + \mu\eta_{yy}\right)u + \left(\frac{\mu}{3}\eta_{xy}\right)v - \eta_x\sigma_x - \eta_y\tau_{xy} \\ \eta_y p + \rho v V_c + \left(\mu\eta_{xx} + \frac{4\mu}{3}\eta_{yy}\right)v + \left(\frac{\mu}{3}\eta_{xy}\right)u - \eta_x\tau_{xy} - \eta_y\sigma_y \end{bmatrix}, \tag{10}$$

$$\mathbf{R}^* = \frac{1}{J}\begin{bmatrix} \theta(\xi_x^2 + \xi_y^2)\rho \\ \left(\frac{4\mu}{3}\xi_x^2 + \mu\xi_y^2\right)u + \frac{\mu}{3}\xi_x\xi_y v \\ (\mu\xi_x^2 + \tfrac{4}{3}\mu\xi_y^2)v + \frac{\mu}{3}\xi_x\xi_y u \end{bmatrix}, \tag{11}$$

$$\mathbf{S}^* = \frac{1}{J}\begin{bmatrix} 2\theta(\xi_x\eta_x + \xi_y\eta_y)\rho \\ 2\left(\frac{4\mu}{3}\xi_x\eta_x + \mu\xi_y\eta_y\right)u + \frac{\mu}{3}(\xi_x\eta_y + \xi_y\eta_x)v \\ 2\left(\mu\xi_x\eta_x + \frac{4\mu}{3}\xi_y\eta_y\right)v + \frac{\mu}{3}(\xi_y\eta_x + \eta_y\xi_x)u \end{bmatrix}, \tag{12}$$

$$\mathbf{T}^* = \frac{1}{J}\begin{bmatrix} \theta(\eta_x^2 + \eta_y^2)\rho \\ \left(\frac{4\mu}{3}\eta_x^2 + \mu\eta_y^2\right)u + \left(\frac{\mu}{3}\eta_x\eta_y\right)v \\ (\mu\eta_x^2 + \tfrac{4}{3}\mu\eta_y^2)v + \left(\frac{\mu}{3}\eta_x\eta_y\right)u \end{bmatrix}. \tag{13}$$

In the above equations J is the Jacobian of the transformation and U_c and V_c are the contravariant velocities along the ξ and η directions[19] and are given by

$$U_c = \xi_x u + \xi_y v, \quad V_c = \eta_x u + \eta_y v. \tag{14}$$

2.2. *Turbulence model*

A two-layer eddy viscosity model based on that of Cebeci and Smith[20] is used to represent the effects of turbulence. The model has been described in Reference 17.

3. TIME-SPLIT GROUP FINITE-ELEMENT FORMULATION

The basic idea behind the group formulation[12] is that separate trial solutions are introduced for the groups of terms, e.g. $\mathbf{F}^*$, $\mathbf{G}^*$, that appear in equation (7). Thus

$$\mathbf{F}^* = \sum_J \mathbf{F}_J^*(t)\phi_J(\xi, \eta), \tag{15}$$

where $\mathbf{F}_J^*(t)$ are the nodal values of $\mathbf{F}^*$ and $\phi_J(\xi,\eta)$ are the known trial functions. A conventional finite-element treatment would require separate trial solutions for each dependent variable in the groups like $\mathbf{F}^*$. In the present study we have used linear Lagrange interpolating functions for $\phi_J(\xi,\eta)$. Although higher-order interpolating functions could be used, the increased connectivity[15] implies a considerable loss of economy, particularly in three dimensions. In addition, the interpolating function must be capable of being split[13] in order to develop the time-split scheme described below. This requirement rules out the use of serendipity trial functions.

Application of a conventional Galerkin finite-element method to equation (7) with trial solutions like (15) produces a system of ordinary differential equations that can be written

$$\mathbf{M}_\xi \otimes \mathbf{M}_\eta \mathbf{q}_t^* + \mathbf{M}_\eta \otimes \mathbf{L}_\xi \mathbf{F}^* + \mathbf{M}_\xi \otimes \mathbf{L}_\eta \mathbf{G}^* - \mathbf{M}_\eta \otimes \mathbf{L}_{\xi\xi} \mathbf{R}^* - \mathbf{L}_\xi \otimes \mathbf{L}_\eta \mathbf{S}^* - \mathbf{M}_\xi \otimes \mathbf{L}_{\eta\eta} \mathbf{T}^* = 0, \tag{16}$$

where $\otimes$ denotes the tensor product.

In equation (16) the components of $\mathbf{F}^*$, $\mathbf{G}^*$ etc. are given by equations (9)–(13), $\mathbf{M}_\xi$ and $\mathbf{M}_\eta$ are directional *mass* operators and $\mathbf{L}_\xi, \mathbf{L}_{\xi\xi}, \mathbf{L}_\eta$ and $\mathbf{L}_{\eta\eta}$ are directional *difference* operators. The various operators are defined as follows:

$$\begin{aligned}
&\mathbf{M}_\xi \equiv \left\{\frac{1}{6}, \frac{1+r_\xi}{3}, \frac{r_\xi}{6}\right\}, \quad \mathbf{M}_\eta^t \equiv \left\{\frac{r_\eta}{6}, \frac{1+r_\eta}{3}, \frac{1}{6}\right\},\\
&\mathbf{L}_\xi \equiv \{-1, 0, 1\}/2\Delta\xi, \quad \mathbf{L}_\eta^t \equiv \{1, 0, -1\}/2\Delta\eta,\\
&\mathbf{L}_{\xi\xi} \equiv \left\{1, -\left(1+\frac{1}{r_\xi}\right), \frac{1}{r_\xi}\right\}\Big/\Delta\xi^2, \quad \mathbf{L}_{\eta\eta}^t = \left\{\frac{1}{r_\eta}, -\left(1+\frac{1}{r_\eta}\right), 1\right\}\Big/\Delta\eta^2.
\end{aligned} \tag{17}$$

These have been defined with respect to Figure 1 for a non-uniform grid in the (ξ,η) plane.

The algebraic expressions resulting from the Galerkin finite-element implementation have been divided by $\Delta\xi\,\Delta\eta$ to give equation (17). The similarity between operators $\mathbf{L}_\xi, \mathbf{L}_{\xi\xi}$ and centred finite-difference operators is apparent. The mass operators, $\mathbf{M}_\xi, \mathbf{M}_\eta$ have the effect of distributing the influence of the difference operators over the neighbouring nodes, i.e. a smoothing effect. Thus, with reference to Figure 1 the expression $\mathbf{M}_\eta \otimes \mathbf{L}_\xi \mathbf{F}^*$ is

$$\frac{r_\eta}{6}[\{\mathbf{F}^*_{\substack{i+1\\j+1}} - \mathbf{F}^*_{\substack{i-1\\j+1}}\}/2\Delta\xi] + \frac{(1+r_\eta)}{3}[\{\mathbf{F}^*_{\substack{i+1\\j}} - \mathbf{F}^*_{\substack{i-1\\j}}\}/2\Delta\xi] + \tfrac{1}{6}[\{\mathbf{F}^*_{\substack{i+1\\j-1}} - \mathbf{F}^*_{\substack{i-1\\j-1}}\}/2\Delta\xi]. \tag{18}$$

The role of the mass operators is considered at greater length elsewhere.[13]

We now develop a time-split algorithm to solve the system of equations (16). Introducing a general three-level evaluation of the time derivative, equation (16) is written

$$\mathbf{M}_\xi \otimes \mathbf{M}_\eta \left[\alpha \frac{\Delta \mathbf{q}^{*n+1}}{\Delta t} + (1-\alpha)\frac{\Delta \mathbf{q}^{*n}}{\Delta t}\right] = \beta\,\mathrm{RHS}^{n+1} + (1-\beta)\,\mathrm{RHS}^n, \tag{19}$$

where

$$\mathrm{RHS} = \mathbf{M}_\eta \otimes \mathbf{L}_{\xi\xi} \mathbf{R}^* + \mathbf{L}_\xi \otimes \mathbf{L}_\eta \mathbf{S}^* + \mathbf{M}_\xi \otimes \mathbf{L}_{\eta\eta} \mathbf{T}^* - \mathbf{M}_\eta \otimes \mathbf{L}_\xi \mathbf{F}^* - \mathbf{M}_\xi \otimes \mathbf{L}_\eta \mathbf{G}^*. \tag{20}$$

In equation (19) α, β are free parameters. The choice $\alpha = 1$ and $\beta = 0{\cdot}5$ gives the Crank–Nicolson scheme and $\alpha = 1{\cdot}5$ and $\beta = 1{\cdot}0$ gives a three-level fully implicit scheme which is used in the present work. Both the schemes are second-order accurate in time but the three-level fully implicit (3LFI) scheme is more robust and gives faster convergence as the steady-state solution is approached.[13]

The equations (19) are non-linear for $\Delta \mathbf{q}^{*t} \equiv \left\{\frac{\Delta\rho}{J}, \frac{\Delta\rho u}{J}, \frac{\Delta\rho v}{J}\right\}$. We introduce a Taylor expansion of the equations about the nth level to linearize them. Thus

$$(\mathrm{RHS})^{n+1} = (\mathrm{RHS})^n + \frac{\partial}{\partial \mathbf{q}^*}(\mathrm{RHS})\Delta \mathbf{q}^{*n+1}, \tag{21}$$

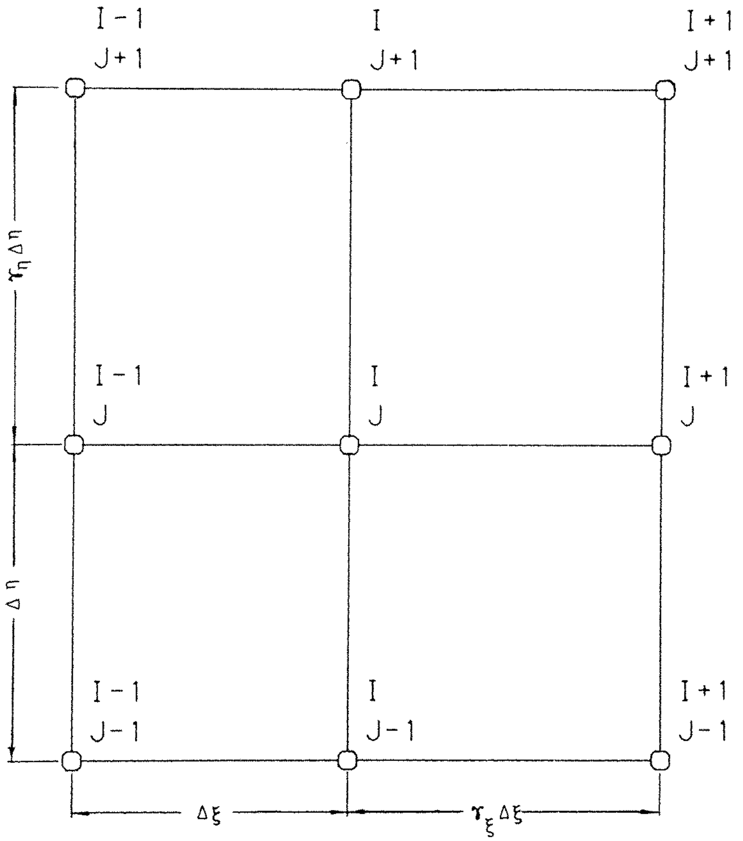

Figure 1. Nodal geometry

where

$$\Delta\mathbf{q}^{*n+1} = \mathbf{q}^{*n+1} - \mathbf{q}^{*n}. \tag{22}$$

Equation (19) is now written as

$$\mathbf{M}_\xi \otimes \mathbf{M}_\eta[\alpha\Delta\mathbf{q}^{*n+1}] - \beta\Delta t\left[\mathbf{M}_\eta \otimes \mathbf{L}_{\xi\xi}\frac{\partial\mathbf{R}^*}{\partial\mathbf{q}^*} + \mathbf{M}_\xi \otimes \mathbf{L}_{\eta\eta}\frac{\partial\mathbf{T}^*}{\partial\mathbf{q}^*} - \mathbf{M}_\eta \otimes \mathbf{L}_\xi\frac{\partial\mathbf{F}^*}{\partial\mathbf{q}^*} - \mathbf{M}_\xi \otimes \mathbf{L}_\eta\frac{\partial\mathbf{G}^*}{\partial\mathbf{q}^*}\right]\Delta\mathbf{q}^{n+1}$$

$$= \Delta t(\mathrm{RHS})^n + \beta\Delta t\mathbf{L}_\xi \otimes \mathbf{L}_\eta\frac{\partial\mathbf{S}^*}{\partial\mathbf{q}^*}\Delta\mathbf{q}^{*n+1} - (1-\alpha)\mathbf{M}_\xi \otimes \mathbf{M}_\eta\Delta\mathbf{q}^{*n}. \tag{23}$$

The term $\beta\Delta t\mathbf{L}_\xi \otimes \mathbf{L}_\eta\frac{\partial\mathbf{S}^*}{\partial\mathbf{q}^*}\Delta\mathbf{q}^{*n+1}$ is due to the cross-derivatives and it may be noted that it does not have any contribution from the implicit grid lines (i,j). Hence the term is calculated explicitly, i.e. $\Delta\mathbf{q}^{*n+1}$ is replaced by $\Delta\mathbf{q}^{*n}$.

Addition of the following term of $O(\Delta t^2)$:

$$\frac{\beta^2\Delta t^2}{\alpha}\left(\mathbf{L}_{\xi\xi}\frac{\partial\mathbf{R}^*}{\partial\mathbf{q}^*} - \mathbf{L}_\xi\frac{\partial\mathbf{F}^*}{\partial\mathbf{q}^*}\right) \otimes \left(\mathbf{L}_{\eta\eta}\frac{\partial\mathbf{T}^*}{\partial\mathbf{q}^*} - \mathbf{L}_\eta\frac{\partial\mathbf{G}^*}{\partial\mathbf{q}^*}\right),$$

to the left-hand side of (23) enables the splitting to be carried out. The split algorithm is implemented as

$$\left[\mathbf{M}_\xi-\frac{\beta}{\alpha}\Delta t\left(\mathbf{L}_{\xi\xi}\frac{\partial\mathbf{R}^*}{\partial\mathbf{q}^*}-\mathbf{L}_\xi\frac{\partial\mathbf{F}^*}{\partial\mathbf{q}^*}\right)\right]\overset{i}{\Delta\mathbf{q}^*}=\frac{\Delta t}{\alpha}(\mathrm{RHS})^{\mathrm{A}}-\left(\frac{1-\alpha}{\alpha}\right)\mathbf{M}_\xi\otimes\mathbf{M}_\eta\Delta\mathbf{q}^{*n}, \tag{24}$$

$$\left[\mathbf{M}_\eta-\frac{\beta}{\alpha}\Delta t\left(\mathbf{L}_{\eta\eta}\frac{\partial\mathbf{T}^*}{\partial\mathbf{q}^*}-\mathbf{L}_\eta\frac{\partial\mathbf{G}^*}{\partial\mathbf{q}^*}\right)\right]\Delta\mathbf{q}^{*n+1}=\overset{i}{\Delta\mathbf{q}^*}, \tag{25}$$

where

$$(\mathrm{RHS})^{\mathrm{A}}=(\mathrm{RHS})^n+\beta\mathbf{L}_\xi\otimes\mathbf{L}_\eta\frac{\partial\mathbf{S}^*}{\partial\mathbf{q}^*}\Delta\mathbf{q}^{*n}. \tag{26}$$

This algorithm is conceptually similar to the first step of a tensor-product approximation to the Newton–Raphson method developed by Baker.^{21}

In equations (24) and (25) the contribution to **R*** etc., arising from the transformation parameters ξ_x, η_x etc., must be evaluated. This is achieved most easily by noting the relationships

$$\xi_x=Jy_\eta,\quad \eta_x=-Jy_\xi,\quad \xi_y=-Jx_\eta\quad\text{and}\quad \eta_y=Jx_\xi, \tag{27}$$

where J is the transformation Jacobian and is given by

$$J=1/(x_\xi y_\eta-x_\eta y_\xi). \tag{28}$$

The following algebraic expressions have been used to evaluate x_ξ etc.:

$$\begin{aligned}
x_\xi&=\Big(x_{\substack{i+1\\ j}}-x_{\substack{i-1\\ j}}\Big)/(1+r_\xi)\Delta\xi,\quad x_\eta=\Big(x_{\substack{i\\ j+1}}-x_{\substack{i\\ j-1}}\Big)/(1+r_\eta)\Delta\eta,\\
x_{\xi\xi}&=\frac{2}{(1+r_\xi)\Delta\xi^2}\left(x_{\substack{i-1\\ j}}-\left(1+\frac{1}{r_\xi}\right)x_{\substack{i\\ j}}+x_{\substack{i+1\\ j}}/r_\xi\right),\\
x_{\eta\eta}&=\frac{2}{(1+r_\eta)\Delta\eta^2}\left(x_{\substack{i\\ j-1}}-\left(1+\frac{1}{r_\eta}\right)x_{\substack{i\\ j}}+x_{\substack{i\\ j+1}}/r_\eta\right),
\end{aligned} \tag{29}$$

and

$$x_{\xi\eta}=\frac{1}{(1+r_\xi)(1+r_\eta)\Delta\xi\Delta\eta}\Big(x_{\substack{i+1\\ j+1}}-x_{\substack{i-1\\ j+1}}-x_{\substack{i+1\\ j-1}}+x_{\substack{i-1\\ j-1}}\Big).$$

Equivalent expressions can be written down for y_ξ etc. in terms of the nodal values, $y_{\substack{i\\ j}}$. Equations (29) can be interpreted as having been obtained by using a lumped Galerkin finite-element formulation with linear Lagrange elements. The similarity with the difference operators in equations (17) is evident.

Equations (24) and (25) are a decoupled implicit local system of equations associated with each grid line in the ξ and η direction. The block tridiagonal system is solved in $O(N)$ operations and there is no need for a global factorization at each time-step.

It may also be noted that $(\mathrm{RHS})^{\mathrm{A}}$ in (24) approaches zero as the steady state is approached. Hence $(\mathrm{RHS})^{\mathrm{A}}$ provides a measure of the 'closeness' of the solution to the steady state. When the steady state is reached $\Delta\mathbf{q}^*=0$, thus indicating that choices for the left-hand side of equations (24) and (25), other than the present one, are possible without altering the steady-state solution.^{16}

4. RESULTS AND DISCUSSION

The time-split finite-element method, described in the previous sections, is used to compute compressible flow past a symmetric trailing edge. Both laminar and turbulent cases are considered. Table I gives the details of the two cases on which Figures 2(a) and 2(b) are based.

Table I

	Laminar	Turbulent
Wedge angle	12·5°	12·5°
Free stream Mach number	0·4	0·4
Reynolds number	100	10^6

Figure 2(a) gives the geometry of the trailing edge. The wedge angle (12·5°) is the same as used in the studies of Viswanath *et al.*[8]

The region AEFG in the physical domain is transformed to a rectangle A′E′F′G′ in the computational domain (Figure 2(b)). The wedge BCD is transformed to a straight line D′C′.

The Blasius profile and the power-law velocity profile were used as the starting data for the laminar and turbulent cases, respectively. The time-steps employed were 0·01 and 0·005 (details regarding the mesh distribution are given later). Typically it required about 1000 time-steps for the laminar flow and 2000 for the turbulent flow before the results converged. Convergence was assumed when the r.m.s. value of the $(\text{RHS})^A$ (see equation (24)) was below 10^{-3}. The execution time for 1000 time-steps (for the mesh employed) for laminar flow was about 15 hrs on a Perkin-Elmer 3220 system. However, this execution time could be reduced with further code development.

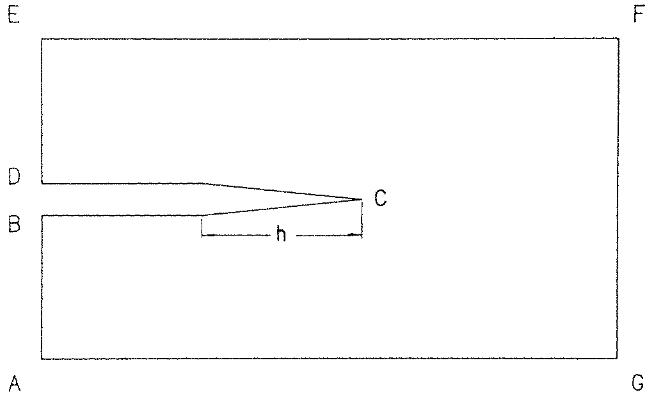

Figure 2(a). Physical domain

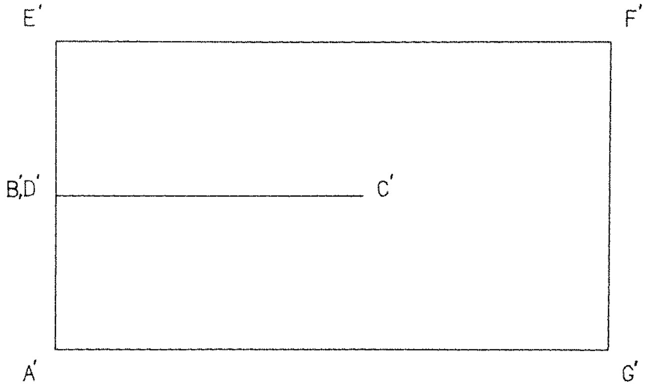

Figure 2(b). Computational domain

4.1. *Boundary conditions*

The following boundary conditions are applied at the various boundaries and solid walls, shown in Figure 2(b).

On solid walls C′D′ the two components of velocity u and v are set to zero. On the inflow boundary A′E′ the velocity components u and v are prescribed from the Blasius profile for the laminar case and from a power-law profile for the turbulent case. Pressure is calculated using the one-dimensional characteristic relation

$$\frac{\partial p}{\partial x} - \rho c \frac{\partial u}{\partial x} = 0, \tag{30}$$

where c is the speed of sound. On the free-stream boundaries E′F′ and A′G′ the values of u and v are prescribed at their non-dimensional free-stream values of 1·0 and 0·0, respectively. Pressure is calculated by a relation similar to (30),

$$\frac{\partial p}{\partial y} - \rho c \frac{\partial v}{\partial y} = 0. \tag{31}$$

On the outflow boundary F′G′ the following conditions on u and v are imposed:

$$\frac{\partial^2 u}{\partial x^2} = \frac{\partial^2 v}{\partial x^2} = 0. \tag{32}$$

Pressure is calculated from the non-reflecting condition

$$\frac{\partial p}{\partial t} - \rho c \frac{\partial u}{\partial x} + \alpha(p - p_\infty) = 0. \tag{33}$$

The non-reflecting condition absorbs the spurious transient signals reaching the boundary and does not allow their reflection into the computational domain. A detailed discussion of this boundary condition is provided in Reference 22. The term $\alpha(p - p_\infty)$ in equation (33) is used only when the steady-state solution is sought. It is found that this extra term can accelerate convergence to the steady state.[23]

4.2. *Laminar Flow*

Computations were carried out for a unit Reynolds number of 100 and a free stream Mach

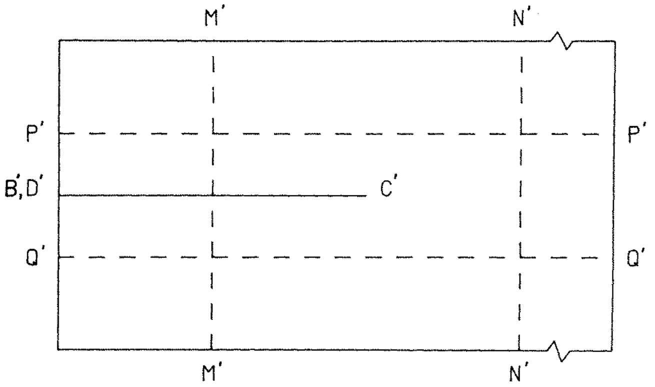

Figure 3. Computational mesh

number of 0·4. The computational domain A′E′F′G′ (Figure 2(b)) was divided into 34 × 42 elements. The mesh in the streamwise direction, i.e. the *x*-direction, was uniform in the region M′M′–N′N′ close to C′ (see Figure 3), the mesh width being 10 per cent of the boundary layer thickness at the inflow boundary DE (Figure 2(a)). In regions upstream of M′M′ and downstream of N′N′ the mesh was stretched geometrically by a factor of 1·3. In the *y*-direction the mesh was uniform in the region P′P′–Q′Q′, outside of which the mesh was stretched geometrically again by a factor of 1·3. The lines P′P′ and Q′Q′ were placed one inlet boundary layer thickness away from D′C′.

The computed *u*-velocity distribution for the symmetric trailing-edge flow is given in Figure 4 for different *x*-stations. The *x*-co-ordinate is normalized with respect to distance, *h* (see Figure 2(a)), and is measured from C. In regions upstream of C the profile is close to that a boundary layer and it undergoes modification downstream of C. In the near wake considerable changes take place close to C only, whereas in the far wake changes are observed all along the profile. The profile at the furthest downstream station indicates that recovery is almost complete.

Figure 5 shows the distribution of the displacement thickness. In regions upstream of the shoulder, the displacement thickness development is similar to that of a flat plate. There is a substantial increase in the displacement thickness in this region due to the growth of the boundary layer. The effect of the trailing-edge geometry is felt from slightly upstream of the shoulder and the displacement thickness increases at a different rate and reaches a peak value at the trailing edge C. In regions downstream of C the displacement thickness decreases and approaches a value higher than that for a flat plate in the far-wake regions.

The surface pressure distribution for the laminar flow over the symmetric trailing edge is given in Figure 6. It is observed that the distribution is close to that for a flat plate except near the trailing edge. The pressure distribution seems to be diffused. The minimum pressure expected at the shoulder occurs downstream of it near the trailing edge. Further an almost discontinuous

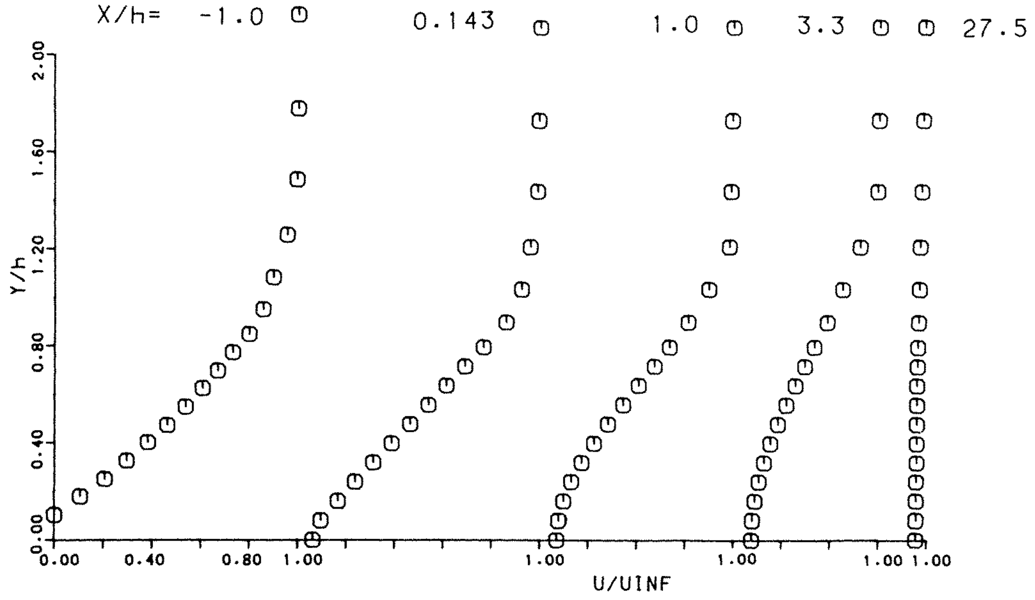

Figure 4. *u*-velocity profiles for laminar flow: $\mathrm{Re} = 100, M_\infty = 0.4$

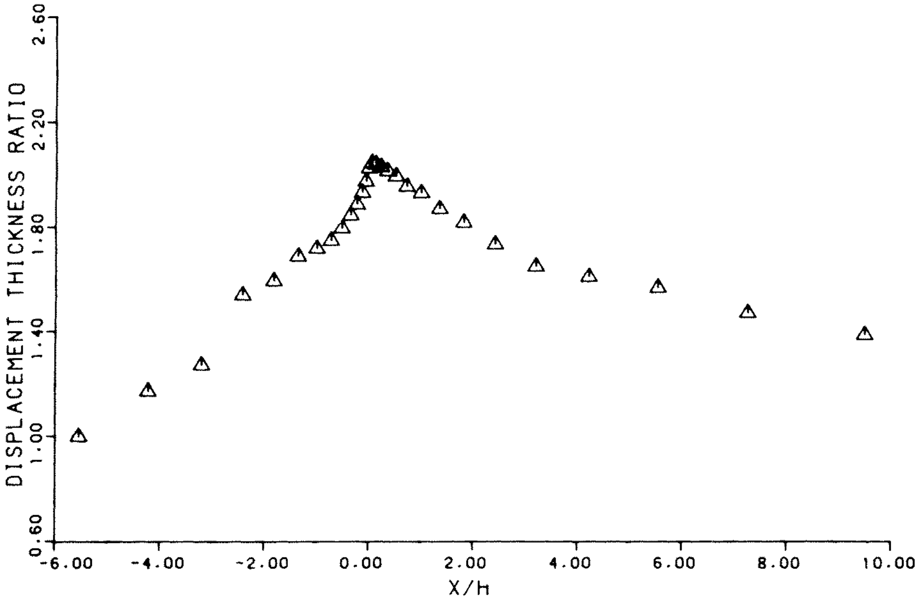

Figure 5. Displacement thickness distribution for laminar flow: Re = 100, $M_\infty = 0.4$. (Displacement thickness is expressed as a ratio of that at the inlet boundary)

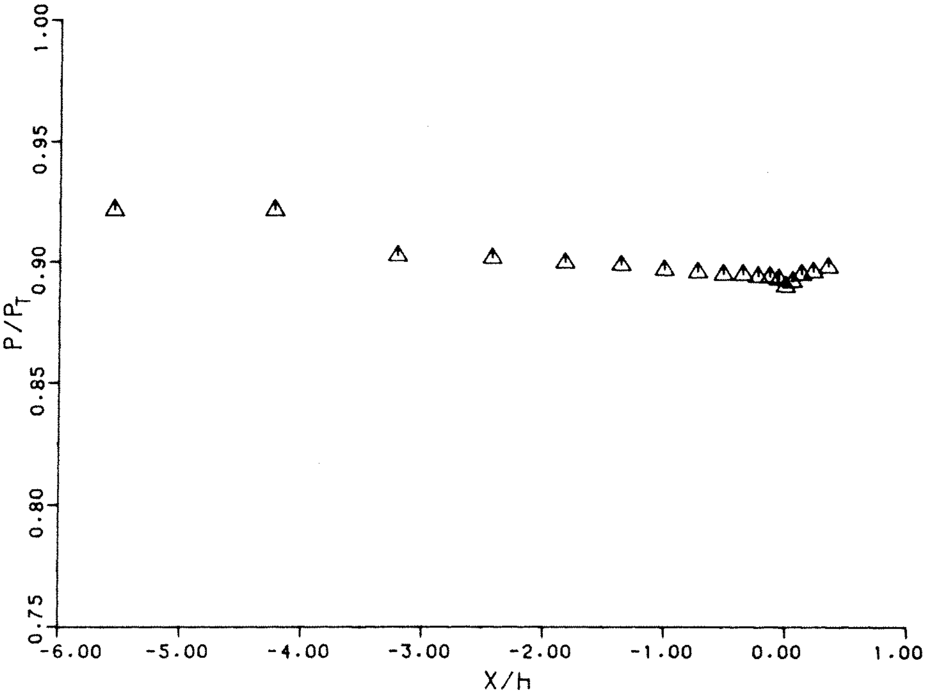

Figure 6. Surface pressure distribution for laminar flow: Re = 100, $M_\infty = 0.4$. (P_T is the total pressure)

jump in pressure is observed far upstream. This jump is caused by the coarseness of the mesh in this region. Computations with a finer mesh indicate that such a jump does not occur. In the absence of any experimental data to compare with, the laminar results are considered statisfactory, i.e. they appear qualitatively plausible.

4.3. Turbulent flow

The computations were carried out for a unit Reynolds number of 10^6 and a free-stream Mach number of 0·4. The computational domain (Figure 2(b)) was divided into 34 × 82 elements. The number of elements in the y-direction had to be more than that for the laminar case to obtain a good resolution of the flow features close to the body. The mesh employed in the x-direction was the same as for the laminar case. But in the y-direction a different type of a mesh was employed. It is well known that in a turbulent flow there is a severe velocity gradient near the wall and a fine mesh is required close to the wall to achieve a good resolution of flow features. The mesh width adjacent to the solid wall was one per cent of the boundary layer thickness at the inlet. This corresponds to $y^+ = 9{\cdot}0$ (y^+ being the 'law-of-the-wall' co-ordinate). The mesh was stretched exponentially from the body surface to the edge of the viscous layer which had 20 elements across it. Outside of the viscous layer the mesh was uniform in the y-direction.

During the course of computations it was found that even such a fine mesh is inadequate. We have, therefore, used the law-of-the-wall approach to determine the velocities at points immediately adjacent to the wall. The law-of-the-wall relations have been described elsewhere.[17]

In the present computations, the turbulence terms such as $(\partial/\partial y)(\varepsilon\partial u/\partial y)$ were calculated as $(\partial^2/\partial y^2)(\varepsilon u)$ to be consistent with group formulation. It may be noted that

$$\frac{\partial^2}{\partial y^2}(\varepsilon u) = \frac{\partial}{\partial y}\left(\varepsilon\frac{\partial u}{\partial y}\right) + u\frac{\partial^2 \varepsilon}{\partial y^2} + \frac{\partial u}{\partial y}\frac{\partial \varepsilon}{\partial y}. \tag{34}$$

The extra terms $u(\partial^2\varepsilon/\partial y^2) + (\partial u/\partial y)(\partial\varepsilon/\partial y)$ in equation (34) are significant only immediately adjacent to the wall and are negligible in regions away from the wall. However, adjacent to the wall, the velocity behaviour was imposed by the law-of-the-wall relations so that the extra terms have no effect on the solution.

The mean u-velocity profiles for various x stations are given in Figure 7(a). Also shown are the profiles obtained by Viswanath *et al.*[8] (It may be noted that the computed and the experimental results in Reference 8 are in good agreement). The x-distances have been normalized with respect to the momentum thickness at the inlet conditions to facilitate comparison of the present results and those of Viswanath *et al.*[8] Further the y-distances have been normalized with respect to the boundary layer thickness at the trailing edge. The present results are seen to be in good agreement with those in Reference 8 along the centreline as well as the inner and outer regions of the wake. Some discrepancies are noticed mainly in the outer layers. These could be attributed to various factors. The Reynolds number considered in the present study is 10^6 whereas Viswanath *et al.* consider a Reynolds number of $26{\cdot}2 \times 10^6$. Further, some inaccuracies in reading of the values of the velocities or y-distances from the figures provided in Reference 8 cannot be ruled out. Figure 7(b) gives separately the mean u-velocity profiles obtained by the present method for various x-stations. Included in Figure 7(b) are the velocity values close to the wall which are omitted from Figure 7(a).

The computed surface pressure distribution around the trailing edge is plotted in Figure 8. Some of the representative points obtained by Viswanath *et al.*[8] are indicated for comparison. In order to facilitate comparison of the results the pressure at the inlet boundary was imposed at the value reported in Reference 8. The agreement again is good except right at the shoulder where the present computation predicts a slightly higher pressure. Further, the recovery of pressure to

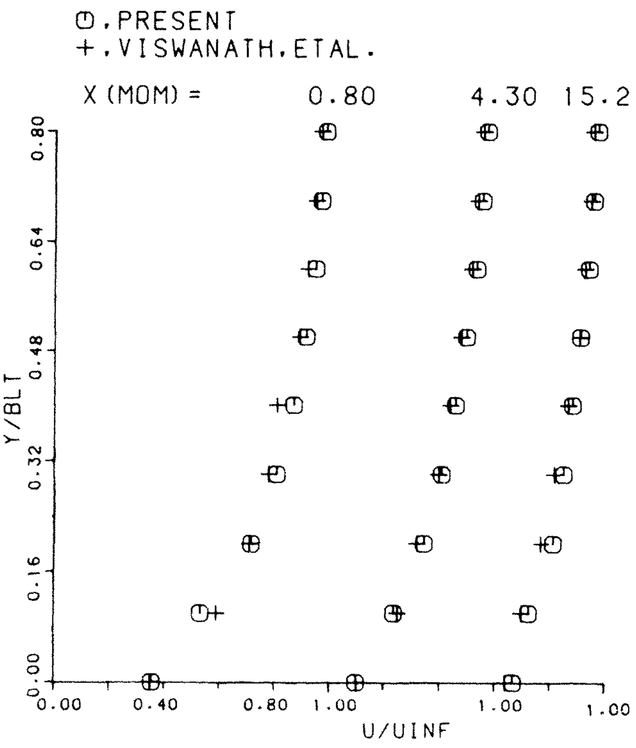

Figure 7(a). Comparison of mean u-velocity profiles for turbulent flow: $\mathrm{Re} = 10^6, M_\infty = 0.4$. (BLT = boundary layer thickness at the trailing edge, MOM = momentum thickness at inlet conditions)

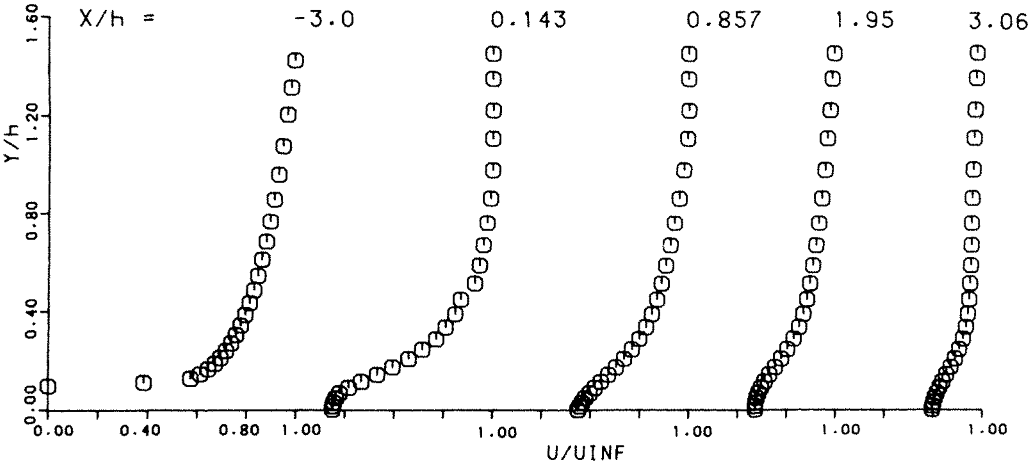

Figure 7(b). Mean u-velocity profiles for turbulent flow: $\mathrm{Re} = 10^6, M_\infty = 0.4$

the flat plate value as the trailing edge is approached is predicted to take place at a lower rate compared to that in Reference 8.

Figure 9 shows the wall shear stress distribution. Wall shear stress in normalized with respect to its value at the inlet conditions. The expression $(\mu + \varepsilon)((\partial u/\partial y) + (\partial v/\partial x))$ was used to calculate the shear stress (and an average value of ε at the wall and the first row of points closest to the

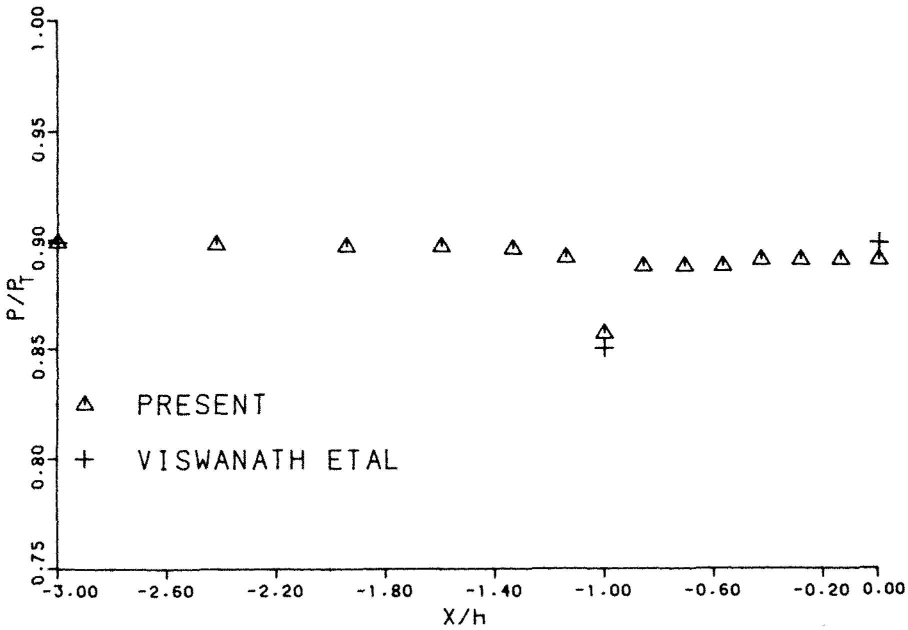

Figure 8. Surface pressure distribution for turbulent flow: $\mathrm{Re} = 10^6, M_\infty = 0.4$. ($P_T$ is the total pressure)

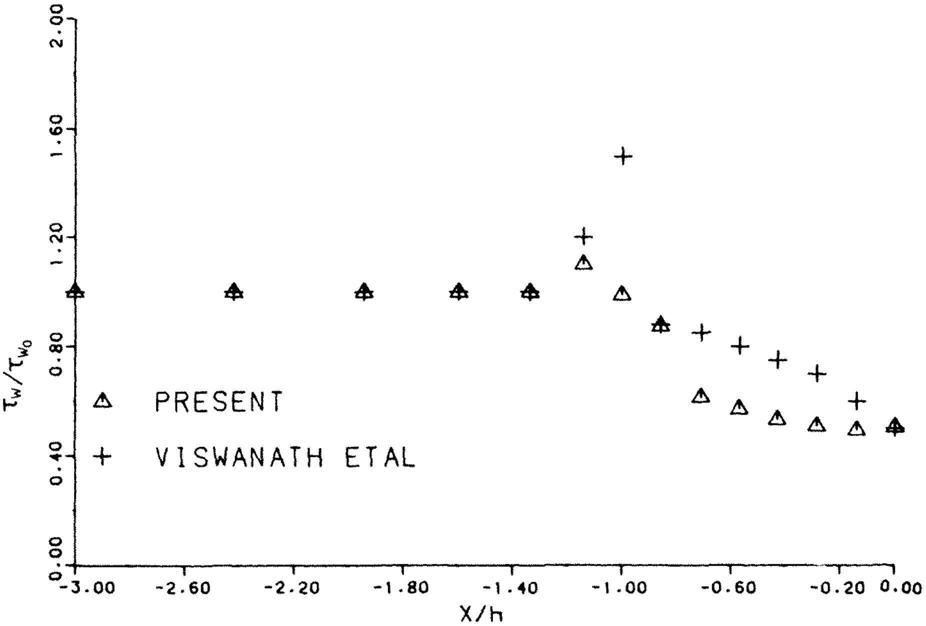

Figure 9. Wall shear stress distribution for turbulent flow: $\mathrm{Re} = 10^6, M_\infty = 0.4$. ($\tau_{\omega 0}$ denotes wall shear stress at inlet conditions)

wall was used). Our computations indicate a gradual decay in shear stress starting slightly upstream of the shoulder, and right at the trailing edge there is a small rise as also observed in Reference 8. At the shoulder, the studies in Reference 8 indicate a substantial rise in shear stress. In our computations such a marked rise was not noticed. Instead the shear stress value rose slightly. The levels reached just upstream of the trailing edge are quite comparable. The comparison of shear stress distribution is made with those computed by Viswanath *et al.*,[8] as the experimental values of wall shear stress are not available.

The displacement thickness distribution for the trailing-edge flow is given in Figure 10. The displacement thickness rises gradually after the shoulder and reaches a peak value at the trailing edge. Downstream of the trailing edge it approaches a constant value of 1·6 which is higher than that at the inlet boundary.

The results for the turbulent flow are thus seen to be in substantial agreement with those of Viswanath *et al.*[8] This agreement demonstrates the capability of the generalized-co-ordinate time-split finite-element method to predict the behaviour of a trailing-edge flow. Further, the effectiveness of the algebraic eddy viscosity model (Section 2.2) to represent the Reynolds shear stress when computing a complex turbulent interaction is also brought out. The results presented here, when considered along with the results for the flat plate and backward-facing step flows in Reference 17, indicate that the algebraic eddy viscosity model can indeed give good results in a variety of situations.

4.4. *Acceleration of convergence*

As stated earlier, it requires around 1000–2000 time-steps before the results converge when

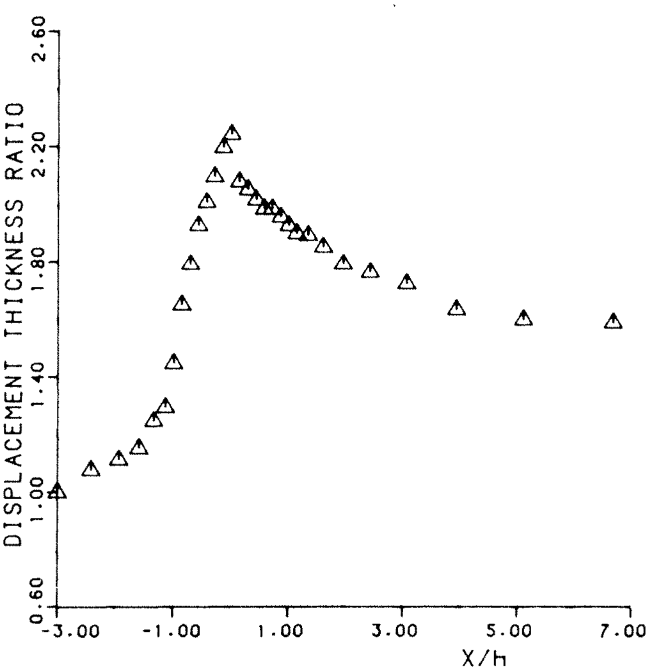

Figure 10. Displacement thickness distribution for turbulent flow: $\mathrm{Re} = 10^6, M_\infty = 0.4$. (Displacement thickness is expressed as a ratio of that at the inlet boundary)

using the method described. To accelerate convergence what is called a 'variable sweep cycle' was developed. The rationale behind such a technique can be explained as follows.

In the example considered it is the trailing edge that effectively controls the flow behaviour. The disturbances to the flow originate at the trailing edge and are subsequently communicated to the other regions of the flow. An inspection of the $(\mathrm{RHS})^{\mathrm{A}}$ values (see equation (24)) showed that it is a maximum near the trailing edge and decreases in regions towards the free-stream and downstream boundaries. This indicates that the region close to the trailing edge has to undergo considerable change before a steady state is attained. Comparatively, the regions near the boundaries have to undergo minor changes.

From a computational point of view this implies that the regions close to the trailing edge require a larger number of iterative sweeps than the regions away from it. A procedure wherein the region close to the body is swept more often than the regions near the free-stream boundary suggests itself. A reduction in execution time is expected from such a 'variable sweep cycle'.

In order to test the procedure the transform plane A′E′F′G′ was divided into three parts—an inner region P′Q′R′S′ of height two boundary layer thickness (P′D′ = D′S′ = one boundary layer thickness) and two outer regions, E′F′Q′P′ and S′R′G′A′ adjacent to free-stream boundaries (Figure 11). Computations were started with one sweep in the entire domain A′E′F′G′. The next two iterations were limited to the inner region P′Q′R′S′. Such a cycle of one sweep in the entire region followed by two sweeps in the inner region was continued until $(\mathrm{RHS})^{\mathrm{A}}$ reduced to a value less than 10^{-3}. Figure 12 shows the r.m.s. value of $(\mathrm{RHS})^{\mathrm{A}}$ plotted against number of time-steps. The convergence is as good as and sometimes better than the full-sweep cycle, though it is slower in the first 400 cycles. After a few hundred cycles, the convergence rate is better. Also shown in Figure 12 is the convergence behaviour when the inner region is swept four times for every sweep in the entire domain. The rate of covergence measured in terms of number of time-steps is less than that for the two-sweep cycle. However, the execution time is reduced considerably in a four-sweep cycle.

A measure of the saving in execution time obtained by using the 'variable sweep' is given by

$$\frac{R_{\mathrm{N}}(1-R_{\mathrm{S}})}{1+R_{\mathrm{N}}} \tag{35}$$

where R_{S} is the ratio of the number of elements in P′Q′R′S′ to that in A′E′F′G′. R_{N} is the additional number of sweeps carried out in P′Q′R′S′ for every sweep in A′E′F′G′. When $R_{\mathrm{N}}=2$, $R_{\mathrm{S}}=\frac{1}{2}$ the saving in execution time is 1/3 and when $R_{\mathrm{N}}=4$ and $R_{\mathrm{S}}=\frac{1}{2}$ the saving is 2/5.

Though the 'variable sweep cycle' gives a considerable reduction in execution time, its applicability seems to be strongly problem dependent. More work is needed before the general methodology

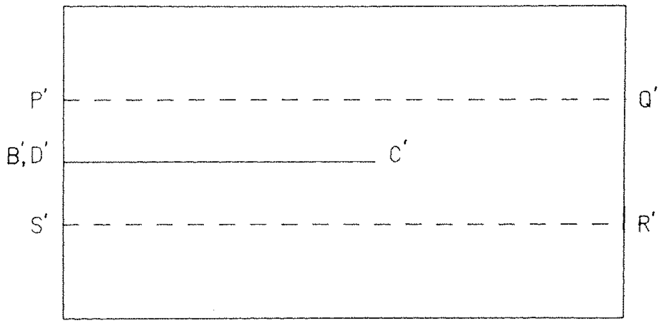

Figure 11. Inner and outer regions for the 'variable sweep cycle'

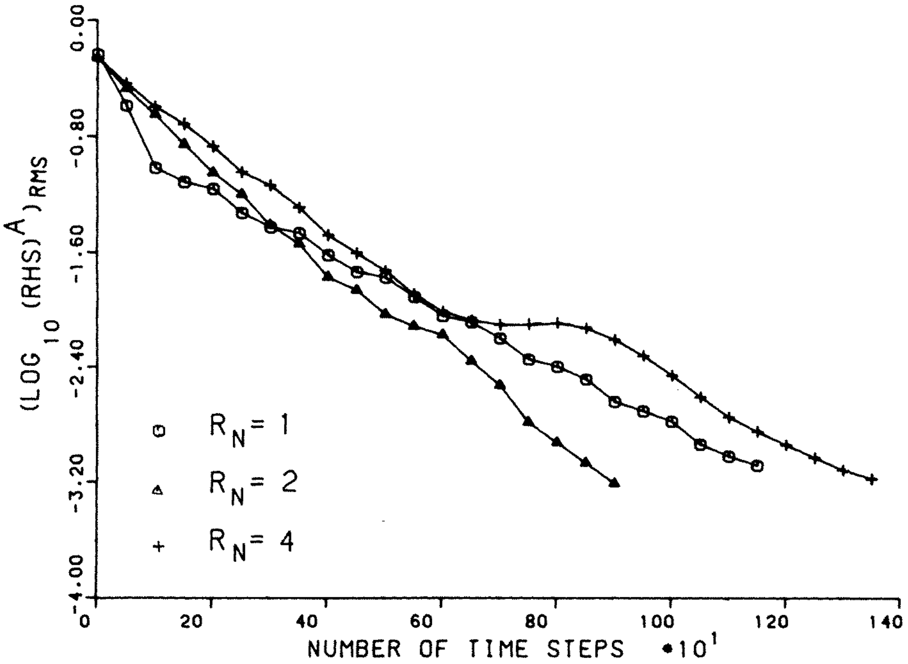

Figure 12. Convergence of the solution for the 'variable sweep cycle'

can be optimized. The effectiveness of the 'variable sweep cycle' suggests that the present solution algorithm would be amenable to a modified multigrid technique.[24]

5. CONCLUSIONS

A time-split group finite-element method in generalized co-ordinates for the computation of viscous flows has been developed. Based on a related formulation applied to two-dimensional Burgers' equation[14] and the stream function and vorticity equations[13] it is expected that the present formulation is more economical than the conventional finite-element method and more accurate than an equivalent finite difference method.

The method is applied to the computation of laminar and turbulent flow past a trailing edge. A two-layer algebraic eddy viscosity model for turbulence is employed. Velocity profiles, displacement thickness distribution for the wake region and the surface pressure distribution appear plausible for the laminar flow results. The results obtained for the turbulent flow are seen to be in good agreement with those presented by Viswanath *et al.*[8] This agreement also implies the validity of an algebraic eddy viscosity model for complicated flows such as the one considered.

A technique to accelerate convergence, called a 'variable sweep cycle', has been described. The technique is shown to be effective in reducing the execution time for the present problem.

ACKNOWLEDGEMENTS

The authors are grateful to the Australian Research Grants Committee for their continued financial support.

REFERENCES

1. C. C. Horstman, 'Numerical simulation of turbulent trailing edge flows', *Second Symposium on Numerical and Physical Aspects of Aerodynamic Flows*, Long Beach, CA, January 1983.
2. C. C. Horstman, 'Prediction of separated asymmetric trailing edge flows at transonic Mach numbers', *AIAA Paper-82-1021*, 1982.
3. R. W. MacCormack, 'A numerical method for solving the equations of compressible flow', *AIAA J.*, **20**, 1275–1281 (1982).
4. G. S. Diewert, 'Computation of turbulent near wake for asymmetric airfoils', *NASA TM 78581*, 1979.
5. R. W. MacCormack, 'An efficient explicit-implicit-characteristic method for solving the compressible Navier–Stocks equations', *SIAM-AMS Proceedings*, **XI**, 1978.
6. A. J. Baker, J. C. Yu, J. A. Orzechowski and T. B. Gatski, 'Prediction and measurement of incompressible turbulent aerodynamic trailing edge flows', *AIAA J.*, **20**, 51–59 (1982).
7. C. M. Rhie and W. L. Chow, 'A numerical study of the turbulent flow past an isolated airfoil with trailing edge separation', *AIAA Paper-82-0998*, 1982.
8. P. R. Viswanath, J. W. Cleary, H. L. Seegmiller and C. C. Horstman, 'Trailing-edge flows at high Reynolds number', *AIAA Paper-79-1503*, 1979.
9. J. W. Cleary, P. R. Viswanath, C. C. Horstman and H. L. Seegmiller, 'Asymmetric trailing-edge flows at high Reynolds number', *AIAA Paper-80-1396*, 1980.
10. P. R. Viswanath and J. L. Brown, 'Separated trailing-edge flow at transonic Mach number', *AIAA Paper-82-0348*, 1982.
11. G. Strang and G. J. Fix, *The Analysis of the Finite Element Method*, Prentice Hall, Englewood Cliffs, N. J., 1973.
12. C. A. J. Fletcher, 'The group finite element formulation', *Comp. Meth. in Appl. Mech. Eng.*, **37**, 225–243 (1983).
13. C. A. J. Fletcher and K. Srinivas, 'Stream function vorticity revisited', *Comp. Meth. Appl. Mech. Eng.*, **41**, 297–322 (1983).
14. C. A. J. Fletcher, 'A comparison of finite element and finite difference solutions of one- and two-dimensional Burgers' equations', *J. Comp. Phys.*, **51**, 159–188 (1983).
15. C. A. J. Fletcher, *Computational Galerkin Methods*, Springer-Verlag, New York, 1983.
16. C. A. J. Fletcher, 'On alternating direction implicit finite element method for flow problems', *Comp. Meth. Appl. Mech. Eng.*, **30**, 307–322 (1982).
17. K. Srinivas and C. A. J. Fletcher, 'Finite element solutions for laminar and turbulent compressible flow', *Int. j. numer. methods fluids*, **4**, 421–439 (1984).
18. O. C. Zienkiewicz, *The Finite Element Method*, 3rd Edn., McGraw Hill, London, 1977.
19. J. L. Steger, 'Implicit finite difference simulation of flow about arbitrary two-dimensional geometries', *AIAA J.*, **16**, 679–686 (1978).
20. T. Cebeci and A. M. O. Smith, *Analysis of Turbulent Boundary Layers*, Academic Press, New York, 1974.
21. A. J. Baker, *Finite Element Computational Fluid Mechanics*, McGraw-Hill, New York, 1983, p. 299.
22. D. H. Rudy and J. C. Strikwerda, 'Boundary conditions for subsonic compressible Navier–Stokes calculations', *Computers and Fluids*, **9**, 327–338 (1981).
23. D. H. Rudy and J. C. Strikwerda, 'A nonreflecting outflow boundary condition for subsonic Navier–Stokes calculations', *J. Comp. Phys.*, **36**, 55–70 (1980).
24. A Brandt, 'Multi-level adaptive solutions to boundary-value problems', *Math Comput.*, **31**, 333–390 (1977).